


M. HAIML   
R. GRANGE  
U. KELLER

# Optical characterization of semiconductor saturable absorbers

Swiss Federal Institute of Technology (ETH) Physics Department/Institute of Quantum Electronics,  
ETH Zurich Hoenggerberg HPT, 8093 Zurich, Switzerland

Received: 24 March 2004

Published online: 3 June 2004 • © Springer-Verlag 2004

**ABSTRACT** Semiconductor saturable absorber mirror (SESAM) devices have become a key component of ultrafast passive mode-locked laser sources. Here we describe in more detail how the key SESAM parameters such as saturation fluence, modulation depth, and nonsaturable losses are measured with a high accuracy. These parameters need to be known and controlled to obtain stable pulse generation for a given laser. A high-precision, wide dynamic range setup is required to measure this nonlinear reflectivity of saturable absorbers. The challenge to measure a low modulation depth and key measures necessary to obtain an accurate calibration are described in detail. The model function for the nonlinear reflectivity is based on a simple two-level travelling wave system. We include spatial beam profiles, nonsaturable losses and higher-order absorption, such as two-photon absorption and other induced absorption. Guidelines to extract the key parameters from the measured data are given.

PACS 07.60.Hv; 42.65.Re; 42.70.Nq

## 1 Introduction

Semiconductor saturable absorber mirror (SESAM) devices have become a key component of ultrafast laser sources [1, 2]. Up to the early 90's, experimental results and theoretical predictions indicated that passively mode-locked diode-pumped solid-state lasers would most likely not operate in continuous-wave mode (without Q-switching), limiting their practical applications. The invention of the first member of the SESAM family in 1992, the anti-resonant Fabry–Pérot saturable absorber, was a breakthrough that allowed for the first demonstration of a passively mode-locked Nd : YLF laser without Q-switching [3]. Since then, we have developed the theoretical basis of the performance of SESAMs in solid-state lasers, worked out design guidelines for application to practical laser systems, and taken this know-how to demonstrate unprecedented laser performance improvements in several key directions: shortest pulse widths [4], highest average and peak power from a passively mode-locked laser [5], and extending the pulse repetition rate to 160 GHz [6]. In addition, SESAMs

could be adjusted to obtain stable Q-switching of compact microchip lasers with pulse durations as short as 37 ps [7], or pulse energies as high as 1.1  $\mu\text{J}$  [8] at a wavelength of around 1  $\mu\text{m}$ . Also in the eye-safe wavelength regime around 1.55  $\mu\text{m}$ , good results [9, 10] have been attained. The results of all this work have also been increasingly commercialized into ultrafast laser products in the last few years. The proper design and characterization of SESAMs is absolutely essential for good performance. The goal of this paper is to address this issue.

We typically integrate the semiconductor saturable absorber into a mirror structure, which results in a device whose reflectivity increases as the incident optical intensity increases. This general class of devices is called semiconductor saturable absorber mirrors (SESAMs) [11]. The main reason for this devices utility is that both the linear and nonlinear optical properties can be engineered over a wide range, allowing for more freedom in the specific laser cavity design. In addition, semiconductor saturable absorbers are ideally suited for passive mode locking solid-state lasers because the large absorber cross section (in the range of  $10^{-14} \text{ cm}^2$ ), and therefore small saturation fluence (in the range of  $10 \mu\text{J}/\text{cm}^2$ ), is ideally suited for suppressing Q-switching instabilities [12]. The key parameters for a saturable absorber are its wavelength range (where it absorbs), its dynamic response (how fast it recovers), and its saturation intensity and fluence (at what intensity and pulse energy density it saturates). Semiconductor materials, combined with proper epitaxial growth and correct optical design of the structure, can achieve a broad range of desired properties for nearly ideal saturable absorber structures for all solid-state lasers. Therefore, it is absolutely essential that a SESAM is correctly characterized to obtain the required parameters such as saturation fluence, modulation depth, nonsaturable absorption, and recovery time. These measurements become even more challenging for SESAMs with small modulation depths of less than 1%. However, precisely such SESAMs are required to push the performance of passively mode-locked solid-state lasers towards higher average power and higher pulse repetition rate because Q-switching instabilities are only suppressed with lower modulation depths.

In this paper we describe in more detail how to correctly determine the key parameters of the SESAMs. Follow-

✉ Fax: +41-1/63-31059, E-mail: haiml@phys.ethz.ch

ing a brief updated overview of SESAM designs (Sect. 2), Sect. 3 gives details about the experimental setup for proper measurement of the nonlinear reflectivity with a high accuracy of  $10^{-4}$  and a dynamic range over four orders of magnitude. Section 4 recalls the standard model for slow absorbers and discusses the extensions made to fit the measurements and extract the key design parameters of the SESAM.

## 2 SESAM designs

At this point we will just give a very brief updated overview of the different SESAM designs. The different designs have different trade-offs and are all still used today for different lasers. Generally a high modulation depth is suited for passive Q-switching [7] and a smaller modulation depth for passive continuous wave (CW) mode locking [12]. The physics behind such a device is based, for the most part, on saturation of the valence-to-conduction band absorption [13]. In the wavelength regime around 800 nm we typically use GaAs, and in the 980 nm to 1.5  $\mu\text{m}$  region InGaAs, and more recently at around 1.3  $\mu\text{m}$  GaInNAs [14, 15] saturable absorber materials.

Initially, semiconductor saturable absorber mirrors for solid-state lasers were used in resonant passive modelocked (RPM) coupled cavities [16, 17], because these early SESAM designs introduced too much loss in the laser cavity (Fig. 1b). In 1992, a solution to this problem resulted in a new type of intracavity saturable absorber mirror, the antiresonant Fabry–Pérot saturable absorber (A-FPSA) [3, 18] where the absorber was integrated inside a Fabry–Pérot structure of which the bottom reflector was a high reflector (Fig. 1c). This was the first intracavity saturable absorber design that allowed for passive mode locking of diode-pumped solid-state lasers without Q-switching instabilities. The Fabry–Pérot was operated at antiresonance to obtain broad bandwidth and low loss. The A-FPSA mirror was mainly based on absorber layers sandwiched between the bottom AlAs/AlGaAs semiconductor and the top  $\text{SiO}_2/\text{TiO}_2$  dielectric Bragg mirror. The top reflector of the A-FPSA provides an adjustable parameter that determines the intensity entering the semiconductor saturable absorber and therefore the saturation fluence of the saturable

absorber device. Thus, this design allowed for a large variation of absorber parameters by simply changing absorber thickness and top reflectors [19, 20]. This resulted in an even simpler SESAM design with a single quantum well absorber layer integrated into a Bragg mirror [21] (Fig. 1d), this was also later referred to as saturable Bragg reflectors (SBRs) [22]. In the 10-femtosecond regime with Ti:sapphire lasers we have typically replaced the lower semiconductor Bragg mirror with a metal mirror to support the required large reflection bandwidth [23, 24]. However, more recently an ultrabroadband monolithically grown fluoride semiconductor saturable absorber mirror was demonstrated that covers nearly the entire gain spectrum of the Ti:sapphire laser. Using this SESAM inside a Ti:sapphire laser resulted in 9.5 fs pulses [25]. The reflection bandwidth was achieved with an AlGaAs/CaF<sub>2</sub> semiconductor Bragg mirror [26].

In 1995 [27] it was further realized that the intracavity saturable absorber can be integrated in a more general mirror structure that allows for both saturable absorption and negative dispersion control, which is now generally referred to as a semiconductor saturable absorber mirror (SESAM) [11] (Fig. 1e). In a general sense we then can reduce the design problem of a SESAM to the analysis of multilayered interference filters for a given desired nonlinear reflectivity response for both the amplitude and phase. The A-FPSA [3, 18], the saturable Bragg reflector (SBR) [21, 22], and the dispersive saturable absorber mirror (D-SAM) [28] are then special examples of SESAM designs. In this more general class of design we do not restrict ourselves to Bragg mirror structures, which are defined by a stack of quarter-wave layers with alternating high and low refractive indices (e.g. [29]). For example, we have demonstrated with many examples that non-quarter-wave layers in mirrors give more design freedom for integrating the absorber layers into the mirror structure. Furthermore, saturable absorbers combined with negative dispersion compensation can be obtained with GTI-type (Gires–Tournois Interferometer) SESAMs [28] or double-chirped semiconductor mirror structures that can provide very broadband negative dispersion [30]. In addition, low field enhancement (LFR) SESAM designs [31, ?] can be used to further reduce saturation fluence without the detrimental effects of strongly resonant structures causing bistability effects and narrower bandwidth. Such a LFR-SESAM design has a low-finesse resonant structure such that the field strength is substantially higher in the spacer layer containing the absorber and therefore reducing the saturation fluence further.

So far the SESAM is mostly used as an end mirror of a standing-wave cavity. Very compact cavity designs have been achieved for example in passively Q-switched microchip lasers [7, 10, 32], and passively mode-locked miniature lasers [33, 34], where a short laser crystal defines a simple monolithic cavity. The SESAM attached directly to the laser crystal then formed one end-mirror of this laser cavity. As the laser cannot be pumped through the SESAM, the laser output needs to be separated from the collinear pump by a dichroic mirror. These examples suggest that there is a need for a device that combines the nonlinear properties of the SESAM with an output coupler. This has been demonstrated before for a passively mode-locked fiber laser [35], and more recently for solid-state lasers [36].

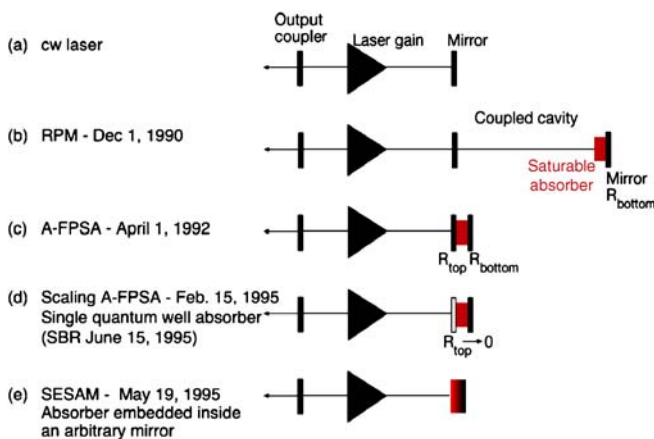
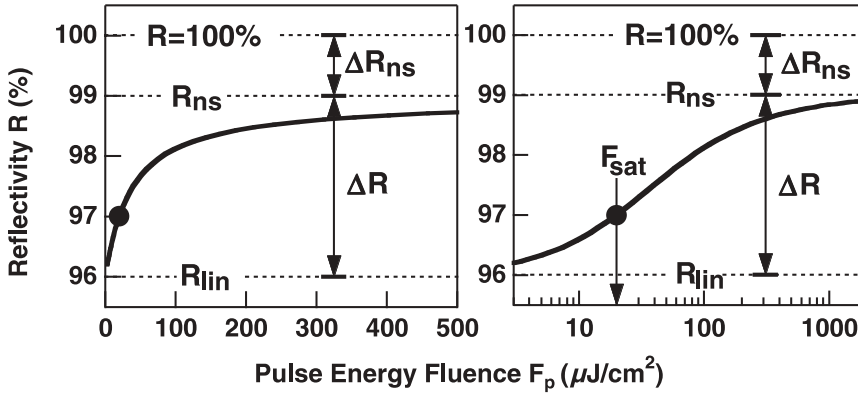


FIGURE 1 Schematics of a CW laser (a) and pulsed lasers (b–e)



**FIGURE 2** Representative characteristic curve: nonlinear reflectivity  $R$  vs. incident pulse energy fluence  $F_p$ . Left: linear scale. Right: logarithmic scale.  $R_{lin}$ : linear reflectivity;  $R_{ns}$ : reflectivity with saturated absorption;  $\Delta R$ : modulation depth;  $\Delta R_{ns}$ : nonsaturable losses in reflectivity;  $F_{sat}$ : saturation (pulse energy) fluence

Semiconductor doped dielectric films have been demonstrated for saturable absorber applications [37]. In this case, InAs-doped thin-film rf-sputtering technology was used which offers similar advantages as SESAMs, i.e. the integration of the absorber into a mirror structure. However, the saturation fluence of more than  $10 \text{ mJ/cm}^2$  is in most cases much too high for stable solid-state laser mode locking. In comparison, epitaxially grown SESAMs typically have saturation fluences in the range of  $10 \text{ } \mu\text{J/cm}^2$  depending on the specific device structure.

### 3 SESAM parameters and Q-switching instabilities

The nonlinear reflectivity  $R$  versus the incident pulse energy fluence  $F_p$  is shown in Fig. 2. For illustration, the same curve is plotted on a linear fluence scale (left) and a logarithmic scale (right). This curve is completely described by three parameters: (i) the linear reflectivity  $R_{lin}$  for pulses with ‘zero’ pulse energy fluence, (ii) the reflectivity  $R_{ns}$  for ‘infinitely’ high pulse energy fluences when all saturable absorption is bleached, and (iii) the saturation fluence  $F_{sat}$ , described in detail later. The modulation depth  $\Delta R$  and the nonsaturable losses  $\Delta R_{ns}$  in reflectivity are defined as:

$$\Delta R = R_{ns} - R_{lin} \quad (1)$$

$$\Delta R_{ns} = 1 - R_{ns}. \quad (2)$$

The definitions above imply that  $R_{lin}$  and  $R_{ns}$  are not experimentally accessible but extrapolated values from the measured data using a proper model function. The significance and stability of these parameters depend on the quality of the model function and will be considered later.

The (pulse energy) fluence  $F_p = \frac{E_p}{A}$  is the incident pulse energy per unit surface area. The saturation fluence  $F_{sat}$  is the fluence required to begin absorption saturation. For an infinitely thin absorber, the reflectivity for a pulse with fluence  $F_p = F_{sat}$  is increased by  $1/e$  (37%) of  $\Delta R$  with respect to  $R_{lin}$ . For bulk absorbers and laser beam profiles other than flat-top deviations from this  $1/e$  relation, may apply. However, for SESAMs this can usually be neglected. Details are given later.

In the picosecond regime in SESAM mode-locked solid-state lasers we have developed a very simple design guideline to prevent Q-switching instabilities [12]:

$$E_p^2 > E_{sat,L} E_{sat,A} \Delta R \quad (3)$$

where  $E_p$  is the intracavity pulse energy,  $E_{sat,L}$  the saturation energy of the laser medium, and  $E_{sat,A}$  the saturation energy of the saturable absorber. Here we assumed a fully saturated, slow saturable absorber that fully recovers between consecutive pulses. More recently, a slightly modified criteria to prevent Q-switching instabilities was introduced [38, 39]:

$$E_p^2 > \frac{E_{sat,A}}{a_2 + 1/E_{sat,L}} \Delta R \quad (4)$$

where we included another nonlinear loss coefficient that increases linearly with the pulse energy with a scaling constant  $a_2$  given by

$$q_2(E_p) = a_2 E_p \quad (5)$$

which includes a certain roll-off at higher fluence (Fig. 3). In the femtosecond regime this roll-off is dominated by two-photon absorption (TPA) for which  $a_2 = \frac{\beta_{TPA} z_{eff}}{\tau_p A_A}$ , where  $\beta_{TPA}$  is the two-photon absorption coefficient,  $z_{eff}$  is the effective TPA-absorber thickness,  $\tau_p$ , and  $A_A$  is the laser mode area on the saturable absorber (for more detailed discussions see Sect. 5). However, we observed a roll-off even in the picosecond regime where TPA is negligible [38].

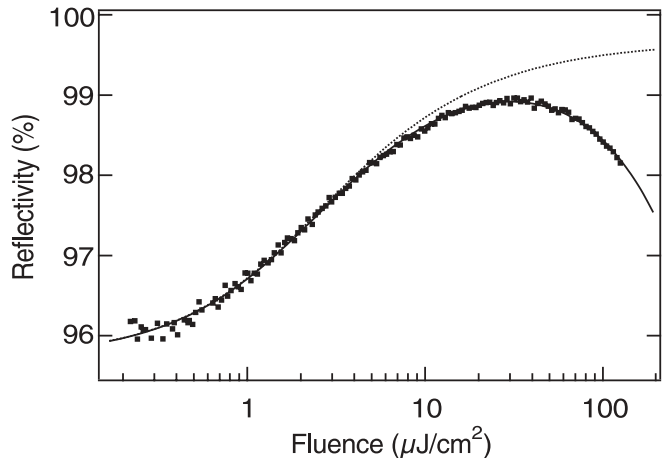


**FIGURE 3** Nonlinear induced absorption for a representative sample. Dots: data, full line: fit-function including nonlinear induced absorption, dotted line: model-function without induced absorption, e.g., longer pulse durations

In the femtosecond regime we have another modification to the criteria (4) given above because soliton formation becomes the dominant pulse forming process, which also suppresses Q-switching instabilities even further. This has been discussed in more detail before but does not change the general trends in (3) and (4).

From (4) and (5) it becomes clear that the detailed parameters are important and have to be known to achieve stable CW mode locking. In addition, based on the same parameters optimization guidelines have been given for Q-switched microchip lasers.

#### 4 High precision wide dynamic range nonlinear reflectivity measurements

##### 4.1 Setup

A well-known technique to measure nonlinear transmission is the single beam  $z$ -scan technique where the sample is moved along the beam axis through the focus of a laser beam [40]. It is a standard technique to measure two-photon absorption coefficients, Kerr, and other nonlinear optical constants. A substantial advantage of the  $z$ -scan technique is that the power of the incident laser beam is kept constant. The variation of incident intensity or fluence (dynamic range) is obtained by moving the sample along the beam axis through a focus. However, this technique cannot be used to measure optical nonlinearities in reflection, as is the case for SESAMs.

Based on our experience the following set-up gives us the most reliable nonlinear reflectivity measurements (Fig. 4). An incident laser beam is focused onto a device under test (DUT in Fig. 4), for example a SESAM. Attenuators control the incident fluence. A beam-splitter feeds a small part of the incident and reflected beam onto two photodiodes. After proper calibration the applied fluence is measured by the photocurrent of the incident photodiode. The reflectivity is calculated from the ratio of the two photodiodes photocurrents. The setup can be divided into five functional groups: (i) an isolated laser source, (ii) power adjustment, (iii) focusing system and DUT holder, (iv) beam-splitter and photodiode optics, and (v) imaging system. This setup allows for measurements of the reflectivity with an accuracy close to  $10^{-4}$  over a dynamic input fluence range of more than 4 orders of magnitude.

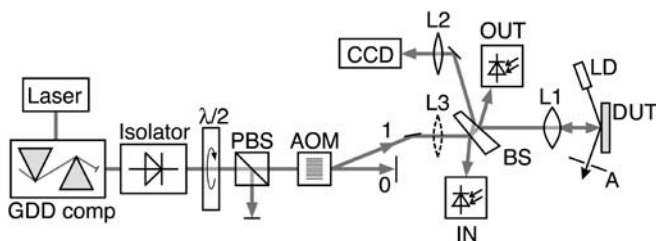


**FIGURE 4** Experimental setup to measure  $R(F)$ . GDD comp: group delay dispersion pre-compensation. Isolator: optical isolator (prevents back-reflection);  $\lambda/2$ : computer controlled, motorized half-wave plate; PBS: polarizing beam splitter; Attenuation ( $\lambda/2 + \text{PBS}$ ): OD 0.01–3.0; AOM: acousto-optic modulator: chopper and attenuation: OD 0.1–3.0; 0,1: zero and first deflection order; BS: low percentage beam splitter; L1: focusing lens; DUT: device under test; LD: laser diode; A: aperture; IN: photodiode incident beam; OUT: photodiode reflected beam; L2: lens, part of imaging system; CCD: imaging laser spot on sample; L3: flip-in “illumination” lens, used for calibration of imaging system

The isolated laser source should match the parameters (wavelength, pulse duration, repetition rates, etc.) of the laser in which the SESAM will be used. Most importantly, this laser has to be stable over time and some effort should be made to start with a good beam quality. As we add a lot of dispersive optics from the laser to the sample, we have to compensate for group delay dispersion (GDD) for measurements with pulse durations below 100 fs. We form an external cavity resonator between the device under test and the laser’s output-coupler. In most cases this will disturb the laser source significantly, especially at the lowest attenuation for highest fluences. Therefore, we have to use an isolator. Otherwise we would have to misalign the setup intentionally to prevent disturbing back-reflections.

A computer-controlled attenuator that operates over 4 orders of magnitude is not a simple task. There are several options available: motorized graded neutral density filters, rotating half-wave plates in combination with a polarizing beam-splitter, an acousto-optical modulator (AOM), or other optics. When using graded neutral density (ND) filters, one has to be careful to avoid thermal lenses inside the ND filters. Rotating half waveplates have the advantages of negligible absorption, but are usually slightly wedged and will cause some disturbing beam steering, which degrades the accuracy of the measurements. An AOM will in principle not change the shape and direction of the diffracted beam. However, thermal effects inside the AOM may appear from different RF powers applied to change the diffraction efficiency. For the latter two, attenuations of about  $10^{-3}$  can be reached easily. Stronger attenuations should be avoided. Operating the half waveplate at stronger attenuations reduces repeatability, makes the measurement sensitive to mechanical vibrations, changes the spectrum of short pulses with broad spectra, and reduces the quality of polarization, which directly affects calibration. For the AOM, stronger attenuation increases amplitude noise in the diffracted beam due to electrical noise at the input side. Therefore we found it convenient to combine both attenuators to increase the dynamic range of our setup. We use the half-waveplate for slower coarse adjustment and the AOM for fast modulation.

We generally use lock-in detection to detect the signals and reject the photodiodes dark currents and environmental background light. In principal one could use a standard chopper. However, for accurate results the beam diameter should be much smaller than the chopper wheel’s slits. The best place to put the chopper is at a focal point of the beam. Otherwise rising and falling edges of the laser power will result in measuring an average reflectivity over a fluence range instead of measuring the reflectivity at a specific fluence. As we already have an AOM in our setup, we also use it as a chopper with negligible edge effects. Variable duty cycles can be used. For larger spot sizes smaller duty cycles reduce the average thermal load on the sample. Finally, higher chopping frequencies, up to some MHz, can be used allowing for shorter integration times. Note that higher chopping frequencies do not reduce laser noise, because the modulation induced sidebands of the lasers noise spectrum is always shifted to the detection frequency.

The device under test is mounted on an  $xyz$ -stage and a mirror mount. Reproducible surface orientation from device

to device is maintained by a tilt control consisting of an alignment laser diode and an aperture. The focusing lens can be implemented as a zoom lens system to allow for variable spot sizes.

The beam-splitter is an uncoated small-angle wedged glass plate. For minimum sensitivity to polarization effects in the sample, the wedge is placed close to normal incidence in an *s*-polarized beam. Using *p*-polarized light at 45 deg or even worse, at the Brewster angle can be problematic. Transfer optics deliver these few percent of reflected beams to large-area photo-detectors for the incident beam “IN” and reflected beam “OUT” (see Fig. 4). The beam diameter on the diodes is preferentially 1/5 of the detector diameter. For larger beam areas the wings of the beam profile are cut off at the edge of the diode making calibration sensitive to beam steering and lensing effects. Small focused spots on the diodes might be the origin of unnoticed local saturation or nonlinear absorption (TPA) at higher  $F_p$  and short pulse durations or deviation from linearity due to inhomogeneities of the detector area (e.g. growth variations, dust particles, etc.). Even though these effects are small, they can limit the accuracy to less than  $10^{-4}$ , sometimes even going unnoticed. To adjust the power level at the diodes, neutral density filter wheels (not shown in Fig. 4) are placed in the transfer optics. The signal of each photodiode is fed into a lock-in amplifier. This discriminates background light and electrical DC offsets. It does not discriminate against scattered light from the setup. Scattered light is coded with the same chopping frequency and will add to the signal in the lock-in amplifiers. Hence, the diodes have to be shielded against scattered light.

The imaging system is used to position the sample in the focal plane and to image bad spots on the surface, etc. It consists of the two lenses L1 and L2 (see Fig. 4) with focal lengths  $f_1$  and  $f_2$ . The magnification is the ratio of  $f_2/f_1$ . Recall that a typical SESAM has a homogeneous flat surface, like any other mirror in the setup. Hence, the image on the CCD is not an image of the beam’s spot on the SESAM surface. However, moving the device under test in the direction of the beam propagation changes the beam size on the CCD camera. Normally the position of lens L1 is fixed and the device under test is moved along the beam axis to obtain a minimum spot size on the device under test (see next in calibration and alignment). The CCD can be placed such that the beam diameter on the CCD is minimal when the sample is placed in the focus (see the calibration and alignment section).

We can make surface irregularities such as scratches, pitches, or dust particles visible if we increase the illuminated area on the sample with an additional lens L3 flipped into the beam (Fig. 4). The focal length  $f_3$  of L3 should be 30–50 times  $f_1$  and placed at a distance of about  $f_3$  in front of L1. Obviously, L3 has to be placed in front of the beam-splitter BS. After calibration the image system can be used to measure the actual spot size, if the beam is collimated between the beam-splitter (BS) and the focusing lens (L1). However, a knife-edge beam-profiler is more reliable.

#### 4.2 Calibration and alignment

Calibration of reflectivity  $R$  and fluence  $F_p$  requires several steps: finding the focal position to place the de-

vice under test, alignment of the tilt-control for reproducible sample positioning, alignment and calibration of the imaging system, determination of the spot size, calibration of the incident power level, and calibration of the reflectivity reading.

For initial alignment the device under test is chosen to be a SESAM with a high modulation depth  $\Delta R$  that is easy to characterize. This SESAM is mounted and tilted to retro-reflect the beam through standard apertures placed in the setup. There should already be an image of the reflected beam on the CCD. L1 is proper aligned when moving the sample in *z*-direction does not change the center position of the image.

The next step is to place the device under test at the focal position of the lens L1. An uncalibrated measurement of  $R(E_p)$  is done to obtain  $R_{lin}$  and  $E_{sat}$  for this position. This measurement is repeated for several *z*-positions to obtain a plot like Fig. 5. At the focal position the value for  $E_{sat}$  reaches a minimum. This procedure also checks for proper alignment of the OUT-path:  $R_{lin}$  should be constant within a Rayleigh range. Otherwise beam clipping occurs which reduces accuracy.  $R_{lin}$  and  $E_{sat}$  do not need to be calibrated for this step.

Once the focal position of the device under test is set correctly the following adjustments should be done: aperture A of the tilt-control (Fig. 4) is adjusted for maximum transmission. The CCD is placed where the image gives the smallest spot. These two alignment checks allow us to move more quickly between different devices under test, otherwise the previously described method of finding the focal position has to be applied every time again.

The fluence on the device under test is proportional to the reading of the IN-signal from the lock-in amplifier  $V_{IN}$ .

$$F_p = c_F \cdot V_{IN}. \quad (6)$$

The calibration factor  $c_F$  is calculated once by

$$c_F = \frac{1}{f_{rep} v \pi w^2} \frac{P_{DUT}}{V_{IN}}, \quad (7)$$

where  $f_{rep}$  is the repetition rate of the laser,  $v$  is the chopping duty cycle, usually 0.5,  $\pi w^2$  is the focal spot area at the position of the sample,  $w$  is the radius for  $1/e^2$  intensity, and  $P_{DUT}$

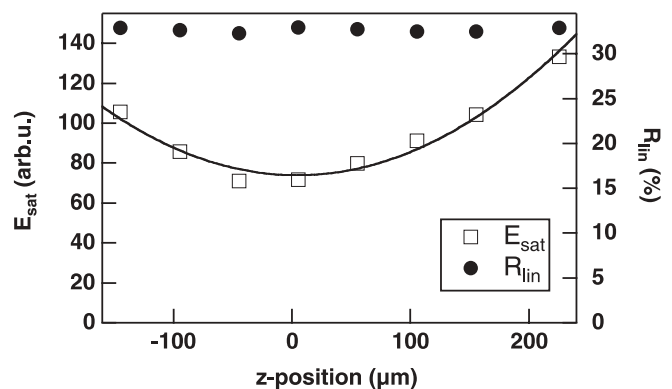


FIGURE 5 Saturation energy  $E_{sat}$  and linear reflectivity  $R_{lin}$  from fit to  $R(F_p)$  data for different *z*-positions. The smallest saturation energy is obtained when the sample is in the focus. The minimum of  $E_{sat}$  is only a valid focal position when  $R_{lin}$  is constant around the minimum. Otherwise some beam clipping occurs which directly affects the value of  $E_{sat}$

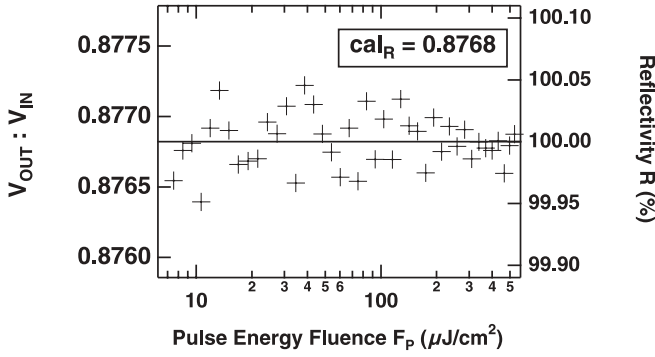


FIGURE 6 Calibration of  $\text{cal}_R$  and sanity check for the flat high-reflector (HR)

is the measured power at the location of the device under test when reading  $V_{\text{IN}}$  from the lock-in. Obviously, the most uncertainty is with the spot size. An error of several percent is quite typical.

More difficult is the calibration of the reflectivity. The reflectivity is given by

$$R(F_p) = c_R \frac{V_{\text{OUT}}}{V_{\text{IN}}}, \quad (8)$$

$c_R$  is obtained by making a measurement with a dielectric high-reflector ( $R = 100\%$ ) as reference. Semiconductor Bragg mirrors are not sufficient because they may show induced absorption. Theoretically,  $c_R$  is a constant. However, using a constant  $c_R$  and plotting  $R(F_p)$  of the high-reflector will never give a perfect 100% flat curve, see e.g. Fig. 6. As sanity check, the high-reflector reference should be measured at the beginning and at the end of every measurement series. The rms deviation is a measure of the possible minimal detectable modulation depth of the setup. Slow drifts in the set-up can cause different calibration factors before and after a measurements series. This will limit the accuracy of the non-linear measurement and should be as small as possible. Based on our experience this sanity check needs to be done.

## 5 Model function

The measured nonlinear reflectivity is used to fit a model function to obtain the key parameters of the saturable absorber. This subsection discusses the model function  $R(F_p)$ . We will show that this model function is well suited to describe the nonlinear behavior of real SESAMs, although a lot of rather strong approximations are made.

We approximate a band-structure by a two-level system, we neglect intraband relaxations as well as trapping or recombination, and we do not include effects of standing wave patterns in the device, carrier diffusion and temperature effects are neglected too. We use a travelling wave model based on rate equations for a two-level system without relaxations, given e.g. in [41, 42]. This is a good approximation for a slow saturable absorber, where the recovery time is longer than the pulse bleaching the absorber [2, 13]. A brief summary of the two-level system is given below.

$$n_1 + n_2 = n \quad (9)$$

$$\dot{n}_1 = -\dot{n}_2 = -(n_1 - n_2) \frac{\sigma}{\hbar\omega} I = -\Delta n \frac{\sigma}{\hbar\omega} I \quad (10)$$

$$\Delta \dot{n} = 2\dot{n}_1 = -\Delta n \frac{2\sigma}{\hbar\omega} I \quad (11)$$

$$\alpha = \sigma \Delta n, \quad \dot{\alpha} = -\alpha \frac{2\sigma}{\hbar\omega} I \quad (12)$$

$n_1$  and  $n_2$ : occupation numbers of level 1 and 2, respectively.

$\sigma$ : absorption and emission cross-section.

$\omega$ : angular frequency of the optical field.

$\alpha$ : absorption coefficient.

A microscopic definition of  $F_{\text{sat}}$  is given by

$$\frac{d\alpha}{dt} = -\frac{\alpha I}{F_{\text{sat}}}. \quad (13)$$

Hence, from (4) and (7) we obtain for the two-level system:

$$F_{\text{sat}} = \frac{\hbar\omega}{2\sigma}. \quad (14)$$

Integration of (13) yields the saturation of absorption  $\alpha$  for times after the pulse has passed:

$$\alpha(F_p) = \alpha_{\text{lin}} \exp\left(-\frac{F_p}{F_{\text{sat}}}\right). \quad (15)$$

To calculate the transmitted pulse energy through a saturable absorber, we have to solve the following system of differential equations:

$$\begin{aligned} \frac{d\alpha(z, t)}{dt} &= -\frac{\alpha(z, t)I(z, t)}{F_{\text{sat}}} \\ \frac{dI(z, t)}{dt} &= -\alpha(z, t)I(z, t). \end{aligned} \quad (16)$$

As mentioned above, we do not take into account standing wave patterns or Fabry–Pérot effects in the SESAM. The reflectivity is calculated as twice the transmission through an absorber of length  $L/2$ . The main difference between the results of a complete transfer matrix calculation and the simple travelling wave approximation is scaling the effective saturation fluence and modulation depth. Fortunately, these deviations scale linearly with the field enhancement factor for the modulation depth and inverse linearly for the saturation fluence [19]. Consequently, from the applied model function, not only macroscopic SESAM parameters can be measured, but also microscopic values for material comparison or SESAM design can be extracted. A somewhat longer derivation of an analytical solution for (13) is given e.g. in [41, 42] yielding the internal transmission for a pulse twice through an absorber of length  $L/2$ .

$$\begin{aligned} R(F_p) &= \frac{F_{\text{OUT}}}{F_{\text{IN}}} = \frac{\int_{-\infty}^{\infty} I(L, t) dt}{\int_{-\infty}^{\infty} I(0, t) dt} \\ &= \frac{\ln(1 + T_{\text{lin}}(e^{F_p/F_{\text{sat}}} - 1))}{F_p/F_{\text{sat}}} \\ &= \frac{\ln(1 + T_{\text{lin}}(e^S - 1))}{S} \end{aligned} \quad (17)$$

with the saturation parameter

$$S = F_p/F_{\text{sat}} \quad (18)$$

Note, that the solution does only depend on the linear transmission  $T_{\text{lin}}$ , and the saturation fluence  $F_{\text{sat}}$ , and not on the specific temporal shape of the intensity. This is true for the limit of a slow absorber with no internal relaxation during the pulse. As mentioned above, for SESAMs, we replace  $T_{\text{lin}}$  with  $R_{\text{lin}}$  in (17).

### 5.1 Nonsaturable Losses

A real absorber device will always show some nonsaturable losses which means that the device will not reach 100% reflectivity, even for arbitrarily high fluences. The origin of these losses are residual transmission losses through the Bragg mirror, scattering losses from rough interfaces, nonsaturable defect absorption [43], free-carrier absorption, Auger recombination, and many more. In most cases they are homogeneously distributed over the absorber layer or transmission losses. These losses can be accounted for by a scaling factor  $R_{\text{ns}}$ .

$$R(F_p) = R_{\text{ns}} \frac{\ln(1 + R_{\text{lin}}/R_{\text{ns}}(e^S - 1))}{S}. \quad (19)$$

Numerical simulations have confirmed that this is valid. For an absorber with very high nonsaturable losses ( $> 10\%$ ), the characteristic curve is still described by (19). Only the apparent  $F_{\text{sat}}$  increases by  $\sqrt{1/R_{\text{ns}}}$ , e.g. for  $R_{\text{ns}} = 90\%$  (99%) we observe only a 5% (0.5%) increase of  $F_{\text{sat}}$  due to losses.

### 5.2 Nonlinear induced absorption

During the years we have observed a deviation from the model function. At higher fluences the reflectivity decreases with increasing fluence according to a second order process like two-photon absorption (TPA), leading to a roll-off in the reflectivity curve (Fig. 3). This additional absorption coefficient increases more or less linearly with fluence (5) and depends on the pulse duration as well [39]. The maximum reflectivity is already reached at a certain fluence and not at the highest possible fluence. In the femtosecond regime the most significant part is due to two-photon absorption in the SESAM structure, not limited to the absorber layer only [44]. However, thermal effects, free-carrier absorption, and other sources of induced absorption also contribute.

From a practical point of view, we take this roll-off into account by multiplying the model function given in (19) with

$$\exp\left(-\frac{F_p}{F_2}\right), \quad (20)$$

which yields excellent results (see Fig. 3).  $F_2$  is the fluence where the SESAM reflectivity has dropped to 37% (1/e) due to induced absorption. A smaller  $F_2$  value corresponds to a stronger roll-off.

The relation between the heuristic device parameter  $F_2$  and the material parameter  $a_2$  from  $q_2(E_p) = a_2 E_p$  (5) in the case of TPA is as follows:

$$q_2(E_p) = \beta I z \approx \beta_{\text{TPA}} \frac{F_p}{\tau_p} z = \beta_{\text{TPA}} \frac{E_p}{\tau_p A_A} z \quad (21)$$

for a TPA coefficient  $\beta_{\text{TPA}}$ , a pulse duration  $\tau_p$ , and a mode area  $A_A$ .

For an absorber of thickness  $z$  the reduced transmission  $T_2$  is given by:

$$T_2(E_p) = \exp(-q_2(E_p)) = \exp(-a_2 E_p). \quad (22)$$

For a real SESAM structure we have to take into account the standing wave pattern, the penetration depth of the optical field into the Bragg mirror, and different two-photon absorption cross-sections for different materials. These effects can be approximated by an 'effective' absorber thickness  $z_{\text{eff}}$ . Note, that most of the TPA in common SESAMs occurs in the spacer layers and the high-index material of the Bragg mirror and only a smaller part in the saturable absorber. Therefore,  $z_{\text{eff}}$  has to be calculated numerically from a given SESAM design.

Combining (21) and (22) results in

$$a_2 = \frac{\beta_{\text{TPA}} z_{\text{eff}}}{\tau_p A_A}. \quad (23)$$

From (20) and (22) we obtain

$$F_2 = (a_2 A_A)^{-1} \approx \frac{\tau_p}{\beta_{\text{TPA}} z_{\text{eff}}}. \quad (24)$$

### 5.3 Finite Spotsize

So far all calculations were done with a constant fluence, i.e. a flattop spot with constant fluence  $F_p$  and radius  $w$ . In this case the fluence  $F_p$  is calculated from the (measured) pulse energy  $E_p$  by:

$$F_p = \frac{E_p}{\pi w^2}. \quad (25)$$

In most applications the laser beam has a Gaussian profile.

$$F_p^{\text{Gauss}}(r) = F_0 \exp(-2r^2/w^2), \quad (26)$$

where  $F_0$  is the peak fluence and  $w$  is the ( $1/e^2$ ) beam radius. The pulse energy  $E_p$  is given by

$$E_p = \int F_p^{\text{Gauss}}(r) 2\pi r dr = \frac{1}{2} F_0 (\pi w^2). \quad (27)$$

Therefore

$$F_p = \frac{1}{2} F_0 = \frac{E_p}{\pi w^2}. \quad (28)$$

The peak fluence in the Gaussian beam is  $2F_p$  and hence saturation already occurs at lower fluences. In the wings of the pulse the fluence and the saturation is much weaker. To calculate the reflectivity for a pulse we have to integrate over the spatial energy distribution.

$$\begin{aligned} R^{\text{Gauss}} &= \frac{E_{\text{OUT}}}{E_{\text{IN}}} \\ &= \frac{1}{E_p} \int_0^\infty 2\pi r dr R(F_p^{\text{Gauss}}(r)) F_p^{\text{Gauss}}(r). \end{aligned} \quad (29)$$

Substituting  $z = 2F_p e^{-\frac{2r^2}{w^2}}$ ,  $dz = -\frac{8r}{w^2} F_p e^{-\frac{2r^2}{w^2}} dr$ :

$$\begin{aligned} R^{\text{Gauss}} &= \frac{1}{E_p} \int_0^{2F_p} dz \frac{\pi w^2}{2} R(z) \\ &= \frac{1}{2F_p} \int_0^{2F_p} dz R(z) = \int_0^1 dz' R(2F_p z'). \end{aligned} \quad (30)$$

Therefore,

$$R^{\text{Gauss}}(F_p) = \int_0^1 dz R^{\text{FlatTop}}(2F_p z) \quad (31)$$

where  $R^{\text{FlatTop}}$  is given by (19) and (20):

$$\begin{aligned} R^{\text{FlatTop}}(x) &= R_{\text{ns}} \frac{\ln(1 + R_{\text{lin}}/R_{\text{ns}}(e^{x/F_{\text{sat}}} - 1))}{x/F_{\text{sat}}} \\ &\times \exp\left(-\frac{x}{F_2}\right). \end{aligned} \quad (32)$$

For good accuracy it is important to fit the measured nonlinear reflectivity to  $R^{\text{Gauss}}(F_p)$  given in (31) and (32).

This is a valid transformation for any function  $R^{\text{Gauss}}(F_p)$  and  $R^{\text{FlatTop}}(F_p)$  as long as lateral diffusion can be neglected.

#### 5.4 Significance of fit-parameters

We only can measure over a finite fluence range. The characteristic parameters are obtained by extrapolating the data to zero and infinitely high fluences by a certain fit-function. The significance of the parameters are directly correlated to the quality of this fit-function. A measure for the quality is (i) the standard deviation of the fit  $\sigma_{\text{Fit}}$  and (ii) the stability of the fit-parameter against different fit ranges.

The standard deviation  $\sigma_{\text{Fit}}$  of a fit  $f(x)$  to a set of data points  $(x_i, y_i)$  is defined by the Gaussian sum as:

$$\sigma_{\text{Fit}} = \sqrt{\frac{1}{N} \sum_{i=1}^N (f(x_i) - y_i)^2}. \quad (33)$$

Figure 7 shows the obtained fit-parameter for different fit ranges. The measured data of a representative sample are plotted in panel (a). These data are fitted in the range  $[F_{\text{min}}, F_{\text{end}}]$ ,  $F_{\text{min}}$  being the lowest measured fluence,  $F_{\text{end}}$  being the variable end-point for the fit.  $\sigma_{\text{Fit}}$ ,  $R_{\text{ns}}$ , and  $F_{\text{sat}}$  are plotted in panel (b)–(d) versus the end-point  $F_{\text{end}}$ , starting at  $F_{\text{end}} \cong F_{\text{sat}}$ . Note that the rms noise level of the data in panel (b) is below 0.1%. For the flattop model (dotted line) a strong increase of  $\sigma_{\text{Fit}}$  is observed for  $F_{\text{end}} > 4F_{\text{sat}}$  and strong variations of  $R_{\text{ns}}$  and  $F_{\text{sat}}$  for  $F_{\text{end}} \in [3F_{\text{sat}}, 10F_{\text{sat}}]$ , a convenient end-point for fitting. These are indications for a poor model function. The Gaussian spot model (straight line) shows significantly lower  $\sigma_{\text{Fit}}$  and only small variations of  $R_{\text{ns}}$  and  $F_{\text{sat}}$  for  $F_{\text{end}} \in [3F_{\text{sat}}, 10F_{\text{sat}}]$ . Figure 7 clearly demonstrates that for a reliable fit of  $R_p(F)$ , the applied fluence  $F_p$  has to reach

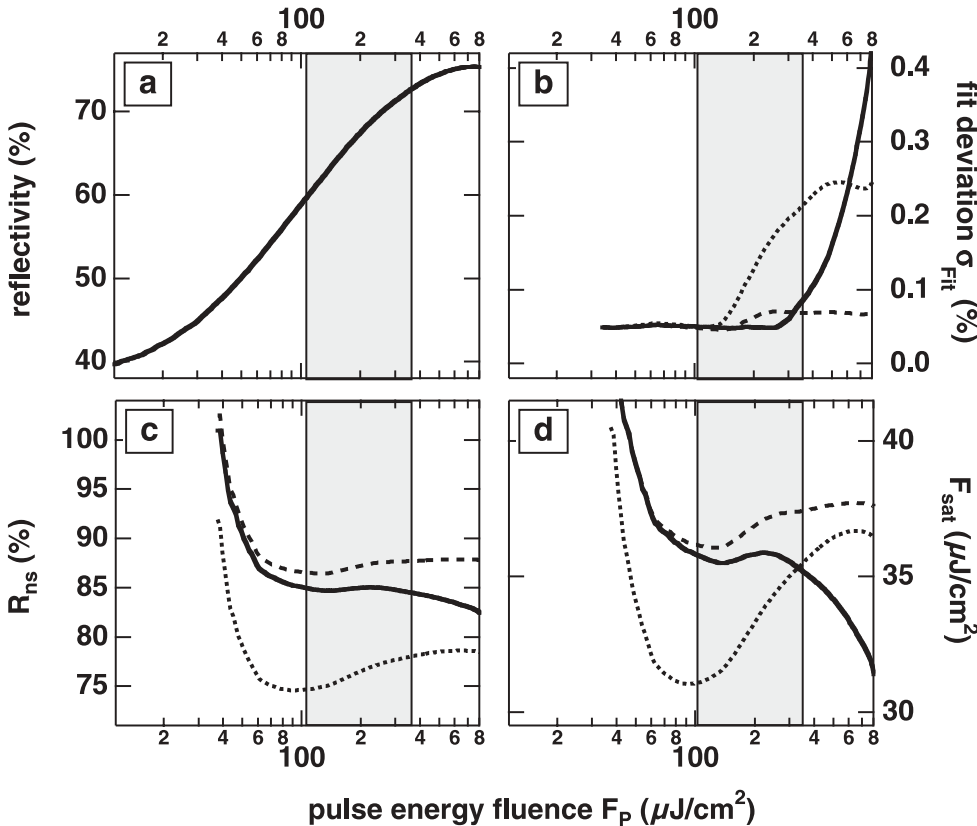


**FIGURE 7** Evaluation of different fit functions for a representative sample. Full lines:  $R_p^{\text{Gauss}}(F_p)$  fit. Dotted lines:  $R_p^{\text{FlatTop}}(F_p)$  fit. Dashed lines:  $R_p^{\text{Gauss}}(F_p)$  fit including TPA. Panel a: reflectivity vs. fluence  $F_p$ . Panels b–d: different fit parameters  $\sigma_{\text{Fit}}$ ,  $R_{\text{ns}}$ , and  $F_{\text{sat}}$  vs. upper limit of fit range. The shaded areas mark the range of 3–10 times  $F_{\text{sat}}$ .



at least  $3F_{\text{sat}}$ . For  $F_{\text{end}} > 10F_{\text{sat}}$  the Gaussian model is also not a proper fit function. The reason is that in the given configuration (830 nm, 150 fs pulses) two-photon absorption (TPA) sets in for higher fluences [44]. This causes a roll-off in panel (a) and is also clearly seen in panel (b). To verify this hypothesis we use the Gaussian model expanded by the heuristic TPA approach of (31) and (32).

In the case of the TPA modified Gaussian model (dashed line),  $F_2$  was fitted for the full fit range in Fig. 7 and kept constant at  $12.5 \text{ mJ/cm}^2$  for the rest. The results show the improvement:  $\sigma_{\text{Fit}}$  increases only slightly above the noise level.  $R_{\text{ns}}$  is somewhat higher because the roll-off is already taken into account by the TPA term. Unfortunately, the TPA extension is not applicable to all data. The fit only yields reliable parameters when the roll-off is clearly observed which is not always the case.

In conclusion, the implementation of a Gaussian spot improves the stability of the fit parameters. However, due to the difference of a semiconductor and a two-level system, the parameters always depend on the applied fit-range.  $F_{\text{sat}}$  is the most sensitive parameter. A reasonable range is to set the endpoint above  $3F_{\text{sat}}$  but below the roll-off from TPA for very high  $F_2$  values or to include a significant part of the roll-off and use the modified fit function from (31) and (32).

## 5.5 Summary

In summary, we have presented a setup to measure nonlinear reflectivity of SESAMs and a model function to fit and interpret measured data. We stressed that measuring small modulation depth samples is not limited by the signal-to-noise ratio, because longer integration times to improve S/N could be applied. The main issues are linearity and accuracy. Special interest was given to proper calibration of the setup. An appropriate model function well describing the saturation behavior was given by (31) and (32), including second order processes. For good accuracy it is important to fit the measured nonlinear reflectivity to this function. From a varying range fitting analysis it becomes clear that the maximum applied fluence should be at least 3 times  $F_{\text{sat}}$  to obtain reliable results. Including induced absorption into the fit-function is necessary for almost all SESAM structures. Measuring samples with modulation depths of less than 1% with sufficient accuracy can be achieved using the measures presented in this paper, but still remains a challenging task.

## REFERENCES

- 1 U. Keller: *Nature* **424**, 831 (2003)
- 2 U. Keller: *Prog. Opt.* **46**, (2004)
- 3 U. Keller, D.A.B. Miller, G.D. Boyd, T.H. Chiu, J.F. Ferguson, M.T. Asom: *Opt. Lett.* **17**, 505 (1992)
- 4 D.H. Sutter, G. Steinmeyer, L. Gallmann, N. Matuschek, F. Morier-Genoud, U. Keller, V. Scheuer, G. Angelow, T. Tschudi: *Opt. Lett.* **24**, 631 (1999)
- 5 E. Innerhofer, T. Südmeyer, F. Brunner, R. Häring, A. Aschwanden, R. Paschotta, U. Keller, C. Hönninger, M. Kumkar: *Opt. Lett.* **28**, 367 (2003)
- 6 L. Krainer, R. Paschotta, S. Lecomte, M. Moser, K.J. Weingarten, U. Keller: *IEEE J. Quant. Elect.* **QE-38**, 1331 (2002)
- 7 G.J. Spühler, R. Paschotta, R. Fluck, B. Braun, M. Moser, G. Zhang, E. Gini, U. Keller: *J. Opt. Soc. Am. B* **16**, 376 (1999)
- 8 G.J. Spühler, R. Paschotta, M.P. Kullberg, M. Graf, M. Moser, E. Mix, G. Huber, C. Harder, U. Keller: *Appl. Phys. B* **72**, 285 (2001)
- 9 R. Fluck, R. Häring, R. Paschotta, E. Gini, H. Melchior, U. Keller: *Appl. Phys. Lett.* **72**, 3273 (1998)
- 10 R. Häring, R. Paschotta, R. Fluck, E. Gini, H. Melchior, U. Keller: *J. Opt. Soc. Am. B* **18**, 1805 (2001)
- 11 U. Keller, K.J. Weingarten, F.X. Kärtner, D. Kopf, B. Braun, I.D. Jung, R. Fluck, C. Hönninger, N. Matuschek, J. Aus der Au: *IEEE J. Sel. Top. Quant. Elect.* **2**, 435 (1996)
- 12 C. Hönninger, R. Paschotta, F. Morier-Genoud, M. Moser, U. Keller: *J. Opt. Soc. Am. B* **16**, 46 (1999)
- 13 U. Siegner, U. Keller: In *Handbook of Optics*, Vol. III, M. Bass (ed.), E.W. Stryland, D.R. Williams, W.L. Wolfe (McGRAW-HILL, NY 2000)
- 14 V. Liverini, S. Schön, R. Grange, M. Haiml, S.C. Zeller, U. Keller: *Appl. Phys. Lett.* **84**, 4002 (2004)
- 15 H.D. Sun, G.J. Valentine, R. Macaluso, S. Calvez, D. Burns, M.D. Dawson, T. Jouhti, M. Pessa: *Opt. Lett.* **27**, 2124 (2002)
- 16 U. Keller, W.H. Knox, H. Roskos: *Opt. Lett.* **15**, 1377 (1990)
- 17 U. Keller, T.H. Chiu: *IEEE J. Quant. Elect.* **QE-28**, 1710 (1992)
- 18 U. Keller: *Appl. Phys. B* **58**, 347 (1994)
- 19 L.R. Brovelli, U. Keller, T.H. Chiu: *J. Opt. Soc. Am. B* **12**, 311 (1995)
- 20 I.D. Jung, L.R. Brovelli, M. Kamp, U. Keller, M. Moser: *Opt. Lett.* **20**, 1559 (1995)
- 21 L.R. Brovelli, I.D. Jung, D. Kopf, M. Kamp, M. Moser, F.X. Kärtner, U. Keller: *Electron. Lett.* **31**, 287 (1995)
- 22 S. Tsuda, W.H. Knox, E. A. d. Souza, W.Y. Jan, J.E. Cunningham: *Opt. Lett.* **20**, 1406 (1995)
- 23 R. Fluck, I.D. Jung, G. Zhang, F.X. Kärtner, U. Keller: *Opt. Lett.* **21**, 743 (1996)
- 24 I.D. Jung, F.X. Kärtner, N. Matuschek, D.H. Sutter, F. Morier-Genoud, Z. Shi, V. Scheuer, M. Tilsch, T. Tschudi, U. Keller: *Appl. Phys. B65*, 137 (1997)
- 25 S. Schön, M. Haiml, L. Gallmann, U. Keller: *Opt. Lett.* **27**, 1845 (2002)
- 26 S. Schön, M. Haiml, U. Keller: *Appl. Phys. Lett.* **77**, 782 (2000)
- 27 U. Keller, D. Kopf: US Patent No. 6466604, (priority date 19 May 1995)
- 28 D. Kopf, G. Zhang, R. Fluck, M. Moser, U. Keller: *Opt. Lett.* **21**, 486 (1996)
- 29 W.H. Knox: US patent No. 5627854 (priority date 15 March 1995)
- 30 R. Paschotta, G.J. Spühler, D.H. Sutter, N. Matuschek, U. Keller, M. Moser, R. Hövel, V. Scheuer, G. Angelow, T. Tschudi: *Appl. Phys. Lett.* **75**, 2166 (1999)
- 31 K.J. Weingarten, G.J. Spühler, U. Keller, L. Krainer: US patent No. 6538298 (priority date 10. Dec. 2001)
- 32 B. Braun, F.X. Kärtner, U. Keller, J.-P. Meyn, G. Huber: *Opt. Lett.* **21**, 405 (1996)
- 33 L. Krainer, R. Paschotta, G.J. Spühler, M. Moser, U. Keller: *Electron. Lett.* **35**, 1160 (1999)
- 34 L. Krainer, R. Paschotta, M. Moser, U. Keller: *Electron. Lett.* **36**, 1846 (2000)
- 35 R.C. Sharp, D.E. Spock, N. Pan, J. Elliot: *Opt. Lett.* **21**, 881 (1996)
- 36 G.J. Spühler, S. Reffert, M. Haiml, M. Moser, U. Keller: *Appl. Phys. Lett.* **78**, 2733 (2001)
- 37 I.P. Bilinsky, J.G. Fujimoto, J.N. Walpole, L.J. Missaggia: *Appl. Phys. Lett.* **74**, 2411 (1999)
- 38 A. Schlatter, S.C. Zeller, R. Grange, R. Paschotta, U. Keller: *J. Opt. Soc. Am. B* **21** (August 2004)
- 39 T.R. Schibli, E.R. Thoen, F.X. Kärtner, E.P. Ippen: *Appl. Phys. B* **70**, 41 (2000)
- 40 M. Sheik-Bahae, A.A. Said, T.-H. Wei, D.J. Hagan, E.W.V. Stryland: *IEEE J. Quant. Elect.* **QE-26**, 760 (1990)
- 41 G.P. Agrawal, N.A. Olsson: *IEEE J. Quant. Elect.* **QE-25**, 2297 (1989)
- 42 A.E. Siegman: *Lasers* (University Science Books, California 1986)
- 43 M. Haiml, U. Siegner, F. Morier-Genoud, U. Keller, M. Luysberg, R.C. Lutz, P. Specht, E.R. Weber: *Appl. Phys. Lett.* **74**, 3134 (1999)
- 44 E.R. Thoen, E.M. Koontz, M. Joschko, P. Langlois, T.R. Schibli, F.X. Kärtner, E.P. Ippen, L.A. Kolodziejski: *Appl. Phys. Lett.* **74**, 3927 (1999)